Modelling of photovoltaic production and electrochemical storage in an autonomous solar drone

Mickael Cosson, Benjamin David, Ludovic Arzel, Philippe Poizot, Ahmed Rhallabi

eScience 2 (2022) 235–241

Contents lists available at ScienceDirect

eScience

journal homepage: www.keaipublishing.com/en/journals/escience

Research Paper

Modelling of photovoltaic production and electrochemical storage in an autonomous solar drone

Mickael Cosson [a,b], Benjamin David [b], Ludovic Arzel [a], Philippe Poizot [a,*], Ahmed Rhallabi [a,*]

[a] Nantes Université, CNRS, Institut des Matériaux de Nantes Jean Rouxel, 2 rue de la Houssinière, 44322, Nantes, France
[b] XSun, 1 Route de la Croix Moriau, 44350, Guérande, France

HIGHLIGHTS

- A simulator has been developed to predict the generation of photovoltaic energy and its storage in Li-ion batteries for an autonomous drone
- The simulator is composed of three main modules: the photovoltaic production, the energy storage unit and the energy management system
- The simulator was built using the Matlab© environment
- The simulator has been validated in real-flight conditions
- A parametric study was performed to show the performance of the drone regarding the weather and geographical conditions

GRAPHICAL ABSTRACT

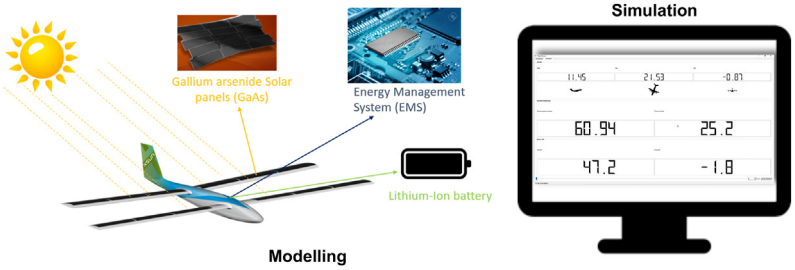

ARTICLE INFO

Keywords:
Unmanned aerial vehicle
Drone flight simulator
Simulation
Energy storage
Photovoltaic energy

ABSTRACT

A simple, efficient simulator has been developed to predict the generation of photovoltaic energy and its storage in Li-ion batteries, for an autonomous drone with four wings covered by solar panels based on thin-film gallium arsenide photovoltaic cells (III–V). This simulator allows prediction of the effective photovoltaic power produced by the solar panels as well as the battery pack voltage when the drone is flying. Flight parameters such as irradiance, sun inclination angles, and drone Euler angles are considered as input parameters. The measured photovoltaic power and battery pack voltage are in good agreement with the simulated values, making practical use by the XSun company possible. This parametric study shows the effects of climatic and geographic conditions on drone autonomy. In optimal weather conditions on a sunny day, drone flight can last 12 h.

1. Introduction

The first generation of drones appeared during World War One, but the very first notions of unmanned aerial vehicles (UAVs) can be traced back to 1849, when balloon carriers were used [1]. Until the end of the last century, drone applications were limited to the military domain, but in the last decade, drone technology has progressed considerably, thanks to a favorable technological environment, and drone applications in civilian life are expanding rapidly [2]. Drones can be used to monitor territories, including marine and river environments. Their deployment

* Corresponding authors.
E-mail addresses: philippe.poizot@cnrs-imn.fr (P. Poizot), ahmed.rhallabi@cnrs-imn.fr (A. Rhallabi).

https://doi.org/10.1016/j.esci.2022.02.004
Received 30 August 2021; Received in revised form 4 January 2022; Accepted 14 February 2022
Available online 18 February 2022

in hostile situations such as forest fires, active volcanoes, storms, earthquakes, and so forth requires the development of UAVs with greater autonomy and longer operation times. Solar UAVs are well suited to address the challenge of achieving longer flights by coupling photovoltaic panels and batteries to power drone operation. High-altitude platforms (HAP), such as the well-known Zephyr 7, have established the current record of more than 14 days, set in July 2010 [3,4]. Other well-known UAVs in the HAP category include Pathfinder, Centurion, and NASA's Helios [3,4]. The prototype SkySailor achieved a 27-h flight in 2008 [5], and in 2015, the AtlantikSolar drone flew 28 h straight [6].

Flight simulation gives a first approximation of drone autonomy with respect to local weather data such as irradiance and temperature, and it can be regarded as the baseline for planning solar UAVs. Optimizing generated solar power remains the primary goal to achieve long flights [7–12], although simulation is also used to design solar drones [5, 13–16].

This paper reports the development of a simple, efficient energy-management simulator, which was then applied to an innovative solar UAV built by the XSun company [17], as described in the Supporting Information (Fig. S1). XSun is one of the first company in the world to design a drone that is autonomous in terms of energy and decision-making. This simulator allows the prediction of the photovoltaic energy produced by the solar panels embedded in the drone wings as well as the battery voltage supply — especially for real-time state-of-charge (SoC) estimation — as a function of the instantaneous flight time. This prediction is achieved by taking into account the GPS flight plan as well as the climatic and geographical conditions. Notably, a simple mathematical formula can be used for each simulator module (photovoltaic, EMS, and battery storage) as a good compromise to obtain an acceptable estimation of our drone's autonomy with a fast run time. We perform parametric studies in terms of climatic and geographic conditions, compare and discuss the simulation results and the measured data from embedded drone sensors in flight.

2. Materials and methods

The simulator was built using the Matlab© environment. Experimental measurements (testing steps) were performed to extract the equivalent parameters of the models for the solar cells and the batteries. In practice, 10 AltaDevices unit solar cells (GaAs) were tested under standard test conditions (STC) using illumination from a Xe lamp normalized at 1000 W/m^2. The temperature was stabilized at 25 °C with a Peltier set-up. The cell was connected to the acquisition device, and the voltage–current curve was collected on a linked computer. Parameter extraction was performed with Matlab©. A repeatable process was performed with the 10 cells. In the energy storage unit, 32 rechargeable unit cells (18650 Li-ion cells) containing the drone's battery pack were electrochemically tested using a VMP potentiostat/galvanostat (Bio-Logic SAS, Seyssinet-Pariset, France). The measurements were performed at 23 °C. The experimental procedures used to obtain the charge/discharge profiles are reported in section D of the Supporting information. The battery pack tests were also performed using a motor test bench with a speed controller to achieve the flight energy-consumption profile.

3. Model formulation

3.1. Irradiance on the wings' surface

The simulator was composed of three main modules: the photovoltaic generator, the energy storage unit (Li-ion batteries), and the energy management system (EMS). The simulator flowchart and EMS algorithm developed in this work are shown in Figs. S2a and S2b, respectively. Prediction of the drone's energy parameters in flight was performed using a pre-established flight plan. The latter was composed of GPS coordinates: Longitude λ_{ecef}, Latitude φ_{ecef}, and inclination angles of the Sun

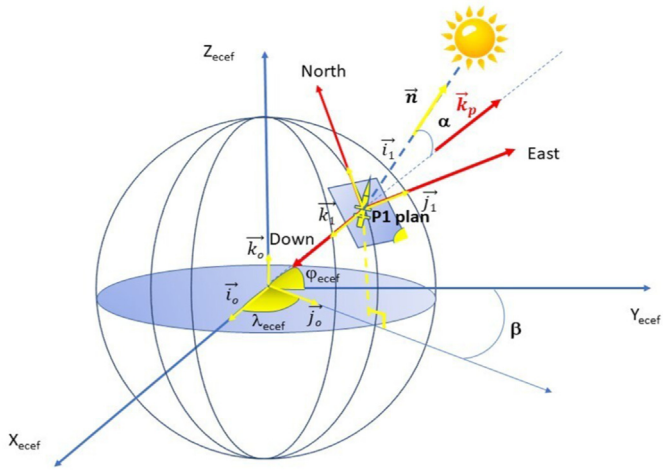

Fig. 1. GPS coordinates of the drone in flight.

α and β relative to the ground. Note that altitude was not considered, since the UAV flies 100 m above ground level (hence, there is negligible effect of altitude on irradiance). The flight plan was completed by the Sun's irradiance, obtained from the satellite database SoDa Helioclim [18], and the Euler angles of the drone: yaw, ψ rotation around the Z axis; pitch, θ rotation around the Y axis; and roll, φ rotation around the X axis. At each time step Δt_i, the photocurrent produced by the photovoltaic panels was determined according to Eq. (1).

$$I_{ph} = \eta\ \vec{n}(t)\ .\ \vec{k_p}(t)\ .\ P_{lig}(t).\ S \tag{1}$$

where η is the coefficient evaluated from the photocurrent's dependence on the irradiance (A/Watt); $\vec{n}(t)$ is the unit vector perpendicular to the earth ground (plan P1); and $\vec{k_p}(t)$ is the unit vector perpendicular to the drone wing surface. In our case, we assume that the drone wing area is flat, so $\vec{k_p}(t)$ is uniform along the wing area. As the flight altitude is low (≈100 m above ground) from the Sun's perspective, the drone is considered to be on the ground (plan P1). $P_{lig}(t)$ is the incident light power density (in W/m^2) on plan P1, and S is the photovoltaic panel surface. The projection of the vectors $\vec{n}(t)$ and $\vec{k_p}(t)$ onto the terrestrial Cartesian coordinate system (X_{ecef} Y_{ecef} Z_{ecef}) (Fig. 1) is given as follows:

$$\vec{k_p}(t) = \begin{bmatrix} \cos(\varphi(t))\sin(\theta(t))\cos(\psi(t)) + \sin(\varphi(t))\sin(\psi(t)) \\ \cos(\varphi(t))\sin(\theta(t))\sin(\psi(t)) - \sin(\varphi(t))\cos(\psi(t)) \\ \cos(\varphi(t))\cos(\theta(t)) \end{bmatrix} \tag{2}$$

$$\vec{n}(t) = \begin{bmatrix} \sin(\alpha(t))\cos(\beta(t)) \\ \sin(\alpha(t))\sin(\beta(t)) \\ \cos(\alpha(t)) \end{bmatrix} \tag{3}$$

3.2. Photovoltaic panel equivalent circuit

The photovoltaic panels (PV) are formed with N_p lines in parallel. Each line is composed of N_s single photovoltaic cells in series (Fig. S3). In the panel equivalent circuit, the contact resistances between the photovoltaic cells are neglected. The irradiance is assumed to be uniform along the surface panels, and all photovoltaic cells are assumed to be identical. By taking these assumptions into account, the voltage on each line V_L is then assumed to be distributed uniformly over N_s cells. Its value on each cell i is therefore $V_i = V_L/N_s$. Each cell is a semiconductor device that, under illumination, produces an electrical current linked to the light intensity [19]. The most widely known equivalent model for a

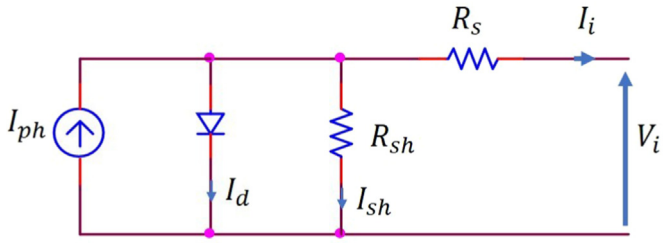

Fig. 2. Photovoltaic cell equivalent circuit, single diode five-parameter model.

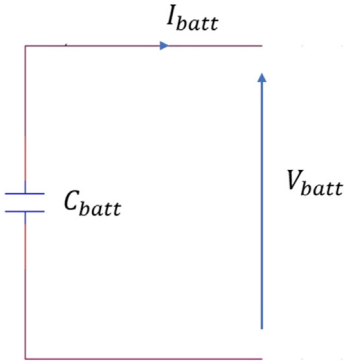

Fig. 3. Ideal capacitor equivalent electric model for the Li-ion batteries being used.

photovoltaic cell is the single diode equivalent circuit, which implies five equivalent parameters (Fig. 2). It is often used in PV system modelling [20–22]. The current I_i on each line (Fig. S3) is determined according to Eq. (4):

$$I_i(V_i) = I_{ph} - I_0\left[\exp\left(\frac{V_i + I_i R_s}{\frac{AkT}{q}}\right) - 1\right] - \left(\frac{V_i + I_i R_s}{R_{sh}}\right) \quad (4)$$

The total current produced by the photovoltaic panels is given by Eq. (5):

$$I_L = N_p \times I_i \quad (5)$$

In these two equations, I_{ph} is the photocurrent generated by the cell; I_0 is the reverse saturation current of the diode; AkT/q is often transformed as AV_t, with $V_t = kT/q$ (the thermal voltage), where k is the Boltzmann constant, q is the electron charge, and T is the temperature of the cell in Kelvin at ambient temperature; A represents the ideality factor of the diode; the two resistances are the series resistance R_s and the shunt resistance R_{sh}; and V_L and I_L are the panel's voltage and current, respectively. The *I–V* electrical characteristic of the single photovoltaic cell i (Fig. S3) is deduced by assuming the shunt resistance R_{sh} value very high [23], thus simplifying the model to four equivalent parameters. So in our simulations, the second term in Eq. (4) was neglected.

Knowing I_{ph}, determined as a function of P_{lig} (Eq. (1)), the maximum power point (MPP) is calculated using the characteristic $I_i(V_i)$ (Eq. (4)). The MPP is therefore calculated at each time step Δt_i and injected as an input parameter into the EMS algorithm (Fig. S2b). The MPP is tracked with this algorithm to ensure the output power of the solar panels used for the load. The difference between the generated solar power P_{pv} and the load P_{load} is used to either charge the batteries if $P_{pv} > P_{load}$ or discharge the batteries if $P_{pv} < P_{load}$. The MPP tracker electronics is neglected, but the direct PV battery coupling is shown to match satisfactorily when the voltage of the photovoltaic panels follows the battery voltage [24]. Moreover, the energy storage unit, acting as a complementary load, ensures that the working point of the photovoltaic panels is well aligned with the maximum power point without the use of MPP tracker electronics [25].

Table 1
Efficiency measurement under 1000 W/m^2 and 25 °C with S_{cell} = 8.5 cm^2.

Sample	V_{OC} (mV)	Isc (A)	Fill Factor (%)	Efficiency (%)
modA1671428045	1110.8	0.223	83.4	24.3
modA1671428047	1114.5	0.223	84.1	24.6
modA1671428056	1113.3	0.225	81.7	24.1
modA1671428057	1117.8	0.223	84.4	24.7
modA1671428058	1113.7	0.222	82.8	24.1
modA1671428059	1118.9	0.226	83.9	25.0
modA1671428060	1121.4	0.224	82.7	24.5
modA1671428062	1118.3	0.225	84.2	25.0
modA1671428063	1119.0	0.227	81.6	24.3
modA1671428064	1107.1	0.224	82.6	24.1

3.3. Equivalent model for the electrochemical energy storage unit: ideal capacitance

Electrochemical models are generally more accurate for modelling the behavior of rechargeable batteries [26,27,28], but they are more computer intensive because complex numerical equations need to be solved. Conversely, the electrical equivalent circuit model is much faster to solve (as the equations are less involved) and can become more complex as the circuit grows in equivalent components to simulate more electrochemical behaviors [29]. Interestingly, based on experimental electrochemical cycling data (reported in section 2.5.), it was possible in the present case to consider as a first approximation the simplest battery model, represented by an ideal capacitance [27] denoted as C_{batt} (Fig. 3).

The charge/discharge of the batteries are governed by Eq. (6):

$$I_{batt} = \pm C_{batt,charge,discharge} \cdot \frac{dV_{batt}}{dt} \quad (6)$$

where I_{batt} and V_{batt} are the current and voltage of the battery, and $C_{batt,charge,discharge}$ denotes the equivalent capacitance of the model for charge and discharge. At each time step, battery charge and discharge are performed at a constant power value:

$$\frac{P_{charge/discharge}}{V_{batt}} = \pm C_{batt,charge,discharge} \cdot \frac{dV_{batt}}{dt} \quad (7)$$

$C_{batt,charge}$ and $C_{batt,discharge}$ are evaluated from the charge/discharge profiles reported in section 2.5.

Solving Eq. (7) knowing $P_{charge/discharge}$ at each time step Δt_i allows us to track the V_{batt} evolution versus the flight time.

3.4. Photovoltaic cell characterization and extraction of electrical parameters

To characterize the solar cells, a representative number of unit cells were also tested under illumination to measure the current versus voltage curves (*I–V*) as well as the efficiency. The cells tested were single-junction GaAs thin-film cells from AltaDevices, encapsulated with a polyethylene terephthalate (PET) film on the drone wings. Table 1 presents characterization results from 10 samples under 1000 W/m^2 illumination at 25 °C:

The efficiency value is very high for a mono-junction thin-film solar cell due to the quality and composition of a cell with a gallium arsenide thin film. The direct bandgap of 1.424 eV is optimal for building high-efficiency solar cells. The efficiency differences between the cells are relatively small, the biggest difference being 0.9%. The as-obtained efficiency values of the solar cells matched the published data from AltaDevices, with a bare efficiency of 27.8% under the same illumination [30] (Figs. S5 and S6). The loss in yield is explained by the PET film encapsulation.

By using a neutral filter, we verify that the current decreases with the illumination intensity. However, the voltage is not affected as much by

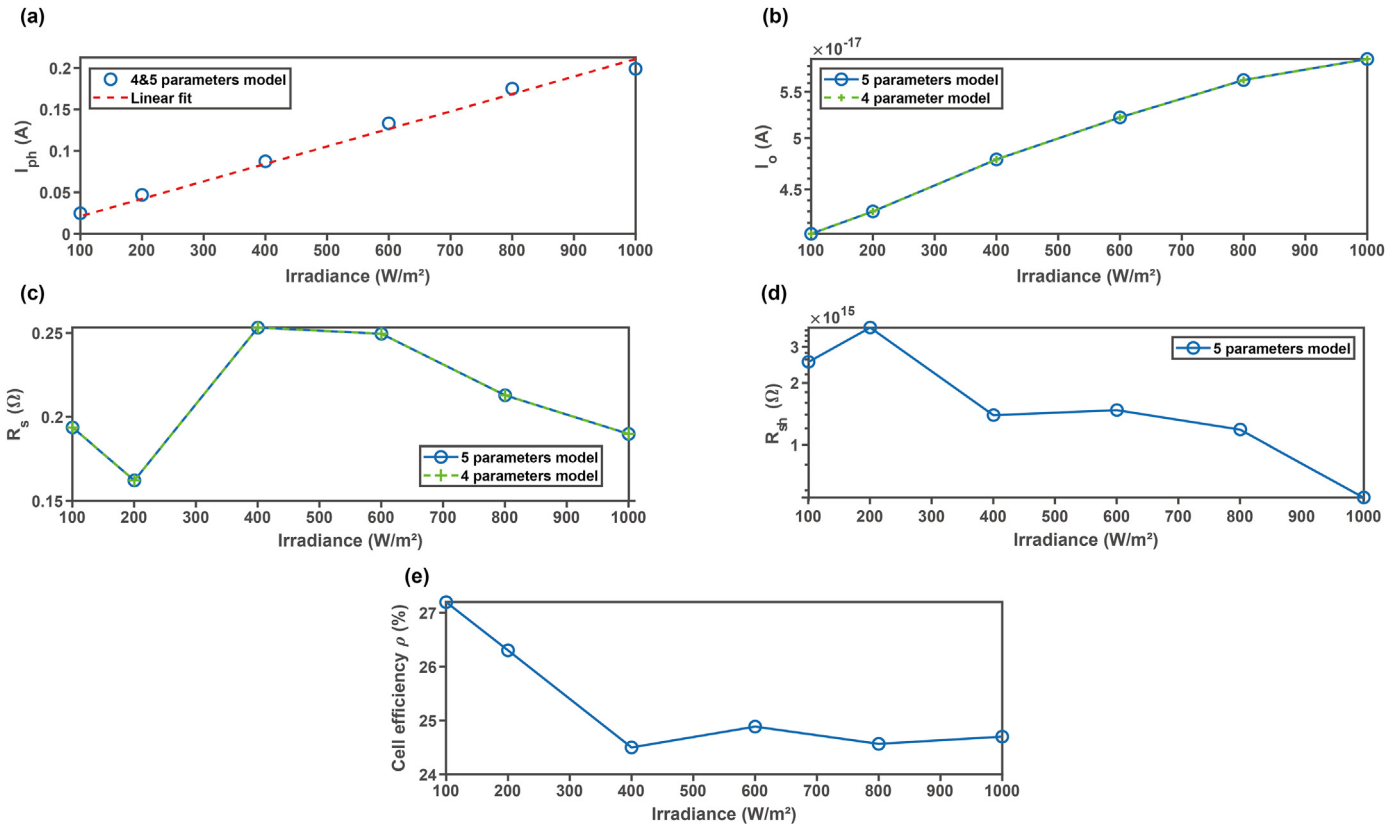

Fig. 4. Evolution of the four- and five-parameter models using the irradiance for a single cell: (a) photo-generated current; (b) reverse current of the diode; (c) series resistance; (d) shunt resistance; (e) cell efficiency.

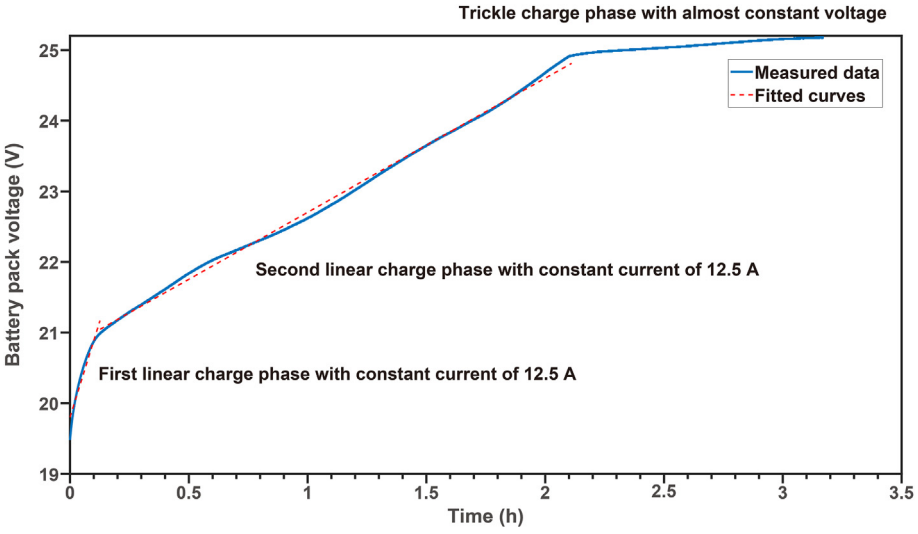

Fig. 5. Constant current battery pack charge at 12.5 A (rate: C/3). Experimental recorded curve (in blue) with the two linear fits (red dashed lines) corresponding to V_{batt_1} and V_{batt_2}, respectively (see text).

low illumination. An example of irradiance variation on a single cell is shown in Fig. S4. From Fig. S4 we can extract the necessary parameters for the five-parameter model (Fig. 2) and a simplified four-parameter model, assuming R_{sh} is infinite. Extraction was performed from the curves reported in Fig. S4 to determine the evolution of the equivalent circuit's parameters (Fig. 2) with illumination. Linear variation of I_{ph} versus the solar power on the cell (Fig. 4a) allows calculation of the η parameter in Eq. (1) ($\eta = 2.04 \times 10^{-4}$ A/W).

The shunt resistance R_{sh} appears to be very large, indicating very few short-circuit losses at the cell's border [31]. The variation in the reverse saturation current I_o is relatively low, between 4.11×10^{-17} A and 5.88×10^{-17} A. The ideality factor is fixed at 1.23, the value averaged from the irradiance measurements. The series resistance R_s is nearly constant. The values of the series resistances at low illumination do not have a detrimental effect on the cell's efficiency. The measured solar cell shows good efficiency within the measurement range (100–1000 W/m^2),

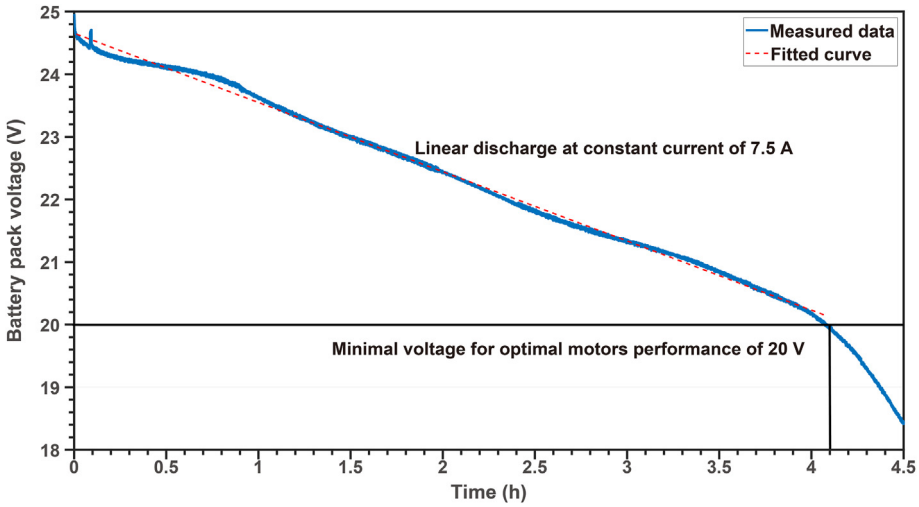

Fig. 6. Constant current battery pack discharge at 7.5 A (rate: C/5). Experimental recorded curve (in blue) with the linear fit (red dashed lines) stopped at 20 V, corresponding approximately to the minimum allowed voltage for a secured flight.

indicating good performance of the AltaDevices solar cells under low illumination. To simplify the equivalent electrical model of the XSun photovoltaic panels, the average values of the other electrical parameters (I_o, A, and R_s) in equation (4) are calculated for the irradiance range 100–1000 W/m^2. The shunt resistance expression is neglected because R_{sh} is considered infinite (Fig. 5e).

3.5. Assessment of Li-ion unit cells, and extraction of electrical parameters

As previously performed with the AltaDevices solar cells, a representative number of Li-ion unit cells constituting the battery pack were first electrochemically assessed using repeated discharge/charge cycles, including at constant power (CPW) (Fig. S8). The experimental details are reported and discussed in section D of the Supporting Information, but with respect to Eq. (7), the corresponding capacitance $C_{batt,charge/discharge}$ can be evaluated. The repeatability process shows that the cells are close to each other (Fig. S8b); the capacitance is thus identical in the model. To validate this roughly linear behavior of the voltage during charge and discharge at the battery pack level, two measurements were performed at a constant current on a battery pack of 66 cells connected in series and parallel, for an assembly of 11 parallel groups of 6 cells in series (i.e., -6S11P). Fig. 5 shows the charge trace obtained at 12.5 A. Note the end of charge is achieved by applying a CV period maintained at ≈25 V.

Such a charge profile can be roughly divided into two main linear steps (Fig. 5), with possible extraction of the corresponding capacitance values.

→ The first step, corresponding to a charge capacity in the first linear domain of 1.6 Ah, is $C_{batt,charge_1} = 4155\,F$.
→ The second step, corresponding to a charge capacity in the second linear domain of 24.8 Ah, is $C_{batt,charge_1} = 23716\,F$.

The total charging capacity is then 26.4 Ah. Note the linear approach cannot be used for the remaining capacity recovered during the last phase (CV), since the current is not constant in this domain. The total charging capacitance is underestimated, but during flight, battery pack

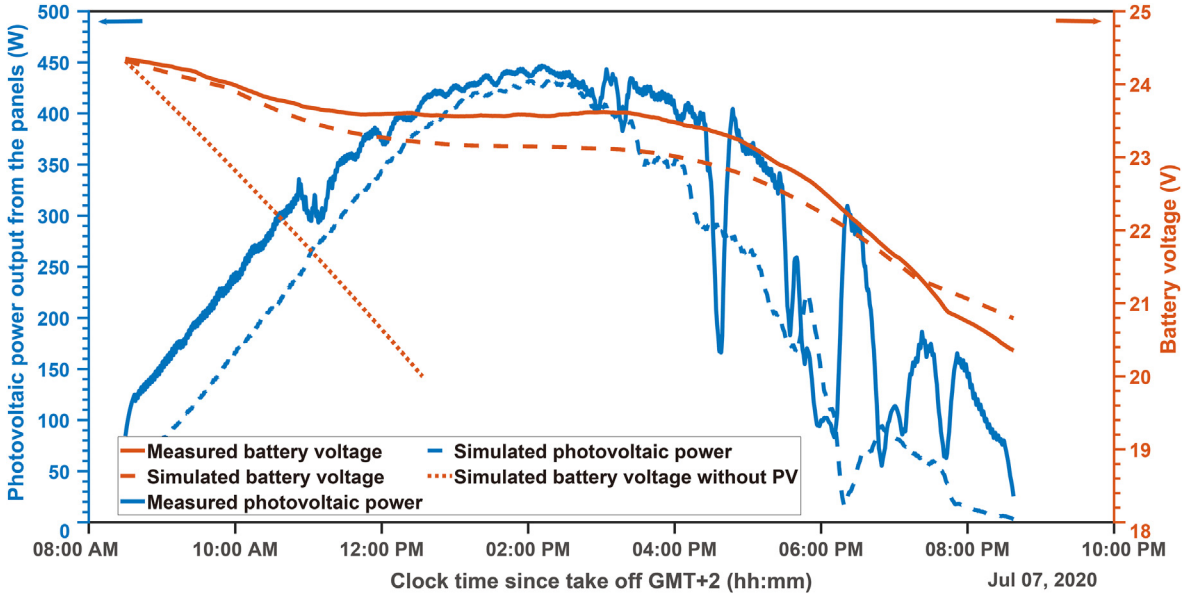

Fig. 7. Comparison of the measured data (solid lines) with the simulated values (dotted lines) from the flight plan with and without photovoltaic electricity generation, both plotted versus time of day (flight time: 12 h; date: July 7, 2020).

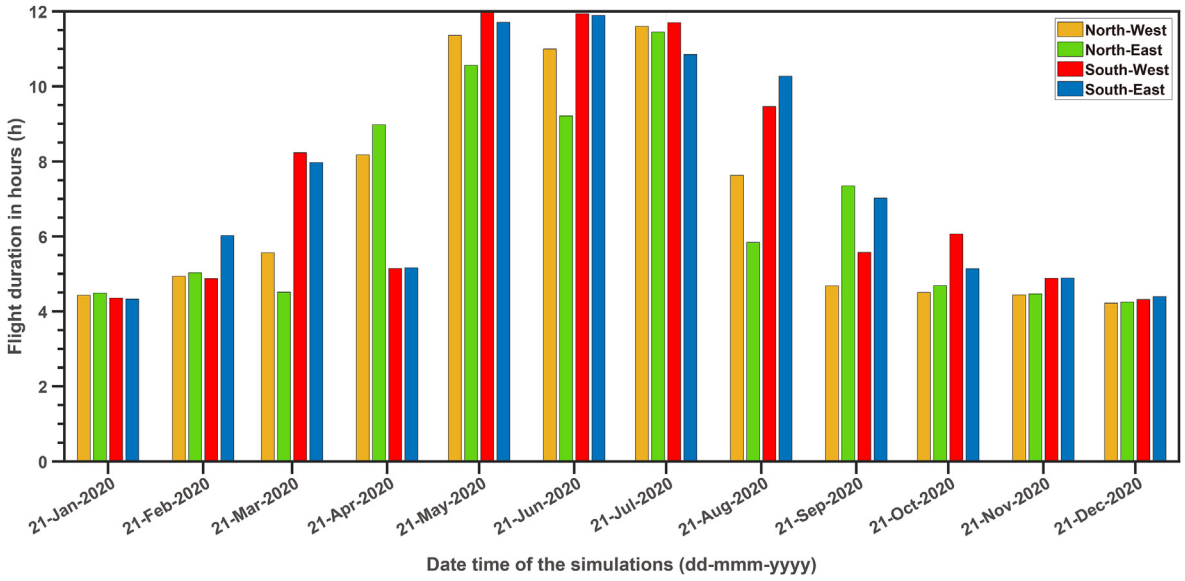

Fig. 8. Distribution of drone autonomy for the four selected regions in France during the 21st day of each month of 2020.

charging is often limited (i.e., the final charging step at CV is not achieved under normal flight conditions).

The same approach was used in discharge (Fig. 6). The discharge step was performed at 7.5 A (C/5). The reference used for the discharge was taken from the cell manufacturer's datasheet. Note that the discharge time was less than the 5 h expected. First, the battery pack used for the tests had already cycled a few times, for measurement on the ground and for in-flight tests in the UAV. Second, the test was performed with a motor and propeller acting as the load; the current needed constant manual adjustment as the voltage was dropping, causing a 30-min delay. The voltage was measured using a battery management system and a CAN communication with a computer.

The linearity covers the majority of the voltage curves for a constant current profile. We end the fit at 20 V, which corresponds to a minimal state of charge SoC_{min} of 20%. The stopping point is just before the end of discharge, where the voltage versus time drops rapidly. The linear regression gives $C_{batt,discharge} = 24405\,F$. This domain corresponds to a discharge capacity of 30.6 Ah.

4. Results and discussion

At this stage of the study, it was necessary to validate the simulator under real flight conditions. Data were therefore extracted from a long endurance flight (flight time of 12 h on July 7, 2020) performed by the XSun drone (Fig. 7). The simulation was run with the exact input of the UAV during the flight, specifically: Euler angles (ψ, θ, φ) from the flight; irradiance during the day, from the satellite database of SoDa Helioclim [18]; and ambient temperature during the day, from the MERRA 2 database [32]. Note the drone flew at a constant speed of 15 m/s, producing an air flow able to cool the panels on the wings. Moreover, the gallium arsenide cells showed quite good performance with respect to temperature [33], as exemplified by the stability of the equivalent parameters shown in Fig. S7. Thereafter, the experimental load profile was injected into the simulator to compare with the calculated values. A mean value of 380 W was measured during the flight, which was a slightly higher than the 300 W obtained from modelling. The difference is mainly explained by the wind conditions; the autopilot adjusted the power to maintain a level flight. Fig. 7 shows the measured and simulated evolution of the solar power and battery voltage during the flight.

It can be seen that the solar power produced was less than the measured value. This difference can be explained by the irradiance model, which neglected the diffuse power portion of the solar rays. An abrupt transition of measured irradiance around 5:30 p.m. and 7:00 p.m. may have been due to the presence of clouds. Voltage underestimation also occurred before the moment when solar power was enough to sustain the flight. During the drone flight, three profiles were observed: the first one corresponded to the flight duration between 8.30 a.m. and 1:00 p.m., when the production of photovoltaic power was not sufficient to operate the drone. At this stage, slow battery discharge was observed to compensate for the lack of photovoltaic power. The second stage, between 1:00 p.m. and 4:00 p.m., corresponded to the time when the Sun was around the zenith (i.e., maximal photovoltaic power production). In this case, the photovoltaic power was sufficient to operate the drone, so the battery was not used and its voltage was roughly constant. After 4:00 p.m., the photovoltaic production decreased with flight time because the Sun moved away from its zenith. In this stage, power production was not sufficient to operate the drone, and additional power from the battery was required. It is worth noting that the stop time for the flight predicted by the simulation agreed well with the measured one.

A simulation was also performed without the photovoltaic panels, showing that the cut-off voltage was reached after only 4 h. The autonomy was therefore tripled thanks to the photovoltaic electricity generation. To study the drone's performance in terms of autonomy evolution versus climatic and geographic conditions, a parametric study was performed by selecting four different regions in France (Table S1 and Fig. 8). More details are reported in section E of the Supporting Information. Fig. 8 shows the as-obtained autonomy performance versus both the weather and the geographic conditions. As expected, the flight durations in northern and southern areas differed, with more pronounced effects during the summer, when a noticeable gain occurred in the South. The disparities are significant in France, with the direct normal irradiance (DNI) between 1200 kWh/m^2/yr in the North compared with 1700 kWh/m^2/yr in the South [34]. However, such disparities are less pronounced in the winter period, as the DNI values are usually low during this season, with short daylight hours and frequent cloudy days. This simulation is therefore able to make a first mapping of the drone's flight duration in France.

5. Conclusion and perspectives

In this study, we developed a simulator built around three models. The electrical model of solar panels was based on a network of photovoltaic cells connected both in series and in parallel. A simple, efficient equivalent electric model was considered for the electrochemical energy

storage unit, based on equivalent capacitances associated with the charging and discharging phases of the battery pack. Output parameters from the simulator were also compared with those of a real flight lasting 12 h. The as-obtained results were judged satisfactory to represent the behavior of this particular UAV during flight. Finally, a parametric study was performed to show the drone's performances in relation to different weather and geographical conditions. The simulation results showed that under optimal weather and geographic conditions, our drone's flight autonomy reached at least 12 h.

Our electrical energy management simulator could be improved using a complete equivalent electric circuit of the battery, such as the double polarization model, for better simulation of battery charge and discharge. In addition, the real morphology of the wing surfaces, which are not flat, could be taken into account to improve prediction of the power produced by the solar panels during flight.

Author contributions

M. Cosson proposed the concept, performed the experiments, built the software, and wrote the original draft. B. David supervised and founded the project. P. Poizot, L. Arzel, and A. Rhallabi provided the methodology, conceptualization, and formal analysis, and supervised and co-wrote the manuscript. A. Rhallabi built the software.

Declaration of competing interest

The authors declare that they have no known competing financial interests or personal relationships that could have appeared to influence the work reported in this paper.

Acknowledgments

This work was funded by the National Agency for Research and Technology (ANRT) through an Industrial Research Convention (CIFRE) between IMN/CNRS UMR 6502 and the XSun company; N° 2018/0079.

Appendix A. Supplementary data

Supplementary data to this article can be found online at https://doi.org/10.1016/j.esci.2022.02.004.

References

[1] B. Custers, The Future of Drone Use: Opportunities and Threats from Ethical and Legal Perspectives, Springer, 2016.
[2] A. Otto, N. Agatz, J. Campbell, B. Golden, E. Pesch, Optimization approaches for civil applications of unmanned aerial vehicles (UAVs) or aerial drones: a survey, Networks 72 (2018) 411–458, https://doi.org/10.1002/net.21818.
[3] F.A. D'Oliveira, F.C.L. de Melo, T.C. Devezas, High-altitude platforms - present situation and technology trends, J. Aerosp. Technol. Manag. 8 (2016) 249–262.
[4] A. Noth, History of Solar Flight, ETH Zurich, July 2008.
[5] A. Noth, PhD Thesis "Design of Solar Powered Airplanes for Continuous Flight", ETH Zurich, 2008.
[6] P. Oettershagen, A. Melzer, T. Mantel, K. Rudin, T. Stastny, B. Wawrzacz, T. Hinzmann, K. Alexis, R. Siegwart, Perpetual flight with a small solar-powered UAV: flight results, performance analysis and model validation, in: 2016 IEEE Aerospace Conference, 2016, pp. 1–8.
[7] A.T. Klesh, P.T. Kabamba, Solar-Powered aircraft: energy-optimal path planning and perpetual endurance, J. Guid. Control Dynam. 32 (2009) 1320–1329.
[8] S. Spangelo, E. Gilbert, A. Klesh, P. Kabamba, A. Girard, Periodic energy-optimal path planning for solar-powered aircraft, in: AIAA Guidance, Navigation, and Control Conference, American Institute of Aeronautics and Astronautics, Chicago, Illinois, 2009.
[9] R. Dai, U. Lee, S. Hosseini, M. Mesbahi, Optimal path planning for solar-powered UAVs based on unit quaternions, in: 2012 IEEE 51st IEEE Conference on Decision and Control (CDC), 2012, pp. 3104–3109.
[10] L. Wirth, P. Oettershagen, J. Ambühl, R. Siegwart, Meteorological path planning using dynamic programming for a solar-powered UAV, in: IEEE Aerospace Conference, 2015, pp. 1–11, 2015.
[11] J. Wu, H. Wang, N. Li, P. Yao, Y. Huang, H. Yang, Path planning for solar-powered UAV in urban environment, Neurocomputing 275 (2018) 2055–2065.
[12] H. Huang, A.V. Savkin, Energy-efficient autonomous navigation of solar-powered UAVs for surveillance of mobile ground targets in urban environments, Energies 13 (2020) 5563.
[13] P. Rajendran, H. Smith, Implications of longitude and latitude on the size of solar-powered UAV, Energy Convers. Manag. 98 (2015) 107–114.
[14] P. Oettershagen, A. Melzer, T. Mantel, K. Rudin, T. Stastny, B. Wawrzacz, T. Hinzmann, S. Leutenegger, K. Alexis, R. Siegwart, Design of small hand-launched solar-powered UAVs: from concept study to a multi-day world endurance record flight, J. Field Robot. 34 (2017).
[15] H. Hwang, J. Cha, J. Ahn, Solar UAV design framework for a HALE flight, Aircraft Eng. Aero. Technol. 91 (2019) 927–937.
[16] S. Jung, Y. Jo, Y.-J. Kim, Flight time estimation for continuous surveillance missions using a multirotor UAV, Energies 12 (2019) 867.
[17] XSun, 2021. https://xsun.fr/. (Accessed 14 October 2021).
[18] P. Blanc, B. Gschwind, M. Lefèvre, L. Wald, The HelioClim project: surface solar irradiance data for climate applications, Rem. Sens. 3 (2011) 343–361.
[19] M.G. Villalva, J.R. Gazoli, E.R. Filho, Comprehensive approach to modeling and simulation of photovoltaic arrays, IEEE Trans. Power Electron. 24 (2009) 1198–1208.
[20] F. Ghani, G. Rosengarten, M. Duke, J.K. Carson, The numerical calculation of single-diode solar-cell modelling parameters, Renew. Energy 72 (2014) 105–112.
[21] C.W. Hansen, Estimation of parameters for single diode models using measured IV curves, in: 2013 IEEE 39th Photovoltaic Specialists Conference (PVSC), IEEE, Tampa, FL, 2013, pp. 223–228.
[22] M. Rasheed, S. Shihab, T. Rashid, Estimation of single-diode model parameters of PV cell, J. Al-Qadisiyah Comput. Sci. Math. 13 (2021) 139–146.
[23] W. Xiao, W.G. Dunford, A. Capel, A novel modeling method for photovoltaic cells, in: 2004 IEEE 35th Annual Power Electronics Specialists Conference (IEEE Cat. No.04CH37551) vol. 3, 2004, pp. 1950–1956.
[24] O. Astakhov, T. Merdzhanova, L.-C. Kin, U. Rau, From room to roof: how feasible is direct coupling of solar-battery power unit under variable irradiance? Sol. Energy 206 (2020) 732–740.
[25] W. Li, J. Zheng, B. Hu, H.-C. Fu, M. Hu, A. Veyssal, Y. Zhao, J.-H. He, T.L. Liu, A. Ho-Baillie, S. Jin, High-performance solar flow battery powered by a perovskite/silicon tandem solar cell, Nat. Mater. 19 (2020) 1326–1331.
[26] J. Newman, K.E. Thomas, H. Hafezi, D.R. Wheeler, Modeling of lithium-ion batteries, J. Power Sources 119–121 (2003) 838–843.
[27] S.M. Mousavi, M. Nikdel, Various battery models for various simulation studies and applications, Renew. Sustain. Energy Rev. 32 (2014) 477–485.
[28] A. Seaman, T.-S. Dao, J. McPhee, A survey of mathematics-based equivalent-circuit and electrochemical battery models for hybrid and electric vehicle simulation, J. Power Sources 256 (2014) 410–423.
[29] H. He, R. Xiong, J. Fan, Evaluation of lithium-ion battery equivalent circuit models for state of charge estimation by an experimental approach, Energies 4 (2011) 582–598.
[30] B.M. Kayes, H. Nie, R. Twist, S.G. Spruytte, F. Reinhardt, I.C. Kizilyalli, G.S. Higashi, 27.6% Conversion efficiency, a new record for single-junction solar cells under 1 sun illumination, in: 2011 37th IEEE Photovoltaic Specialists Conference, 2011, pp. 4–8.
[31] Md.N.I. Sarkar, Effect of various model parameters on solar photovoltaic cell simulation: a SPICE analysis, Renewables 3 (2016) 13.
[32] R. Gelaro, W. McCarty, M.J. Suárez, R. Todling, A. Molod, L. Takacs, C.A. Randles, A. Darmenov, M.G. Bosilovich, R. Reichle, K. Wargan, L. Coy, R. Cullather, C. Draper, S. Akella, V. Buchard, A. Conaty, A.M. da Silva, W. Gu, G.-K. Kim, R. Koster, R. Lucchesi, D. Merkova, J.E. Nielsen, G. Partyka, S. Pawson, W. Putman, M. Rienecker, S.D. Schubert, M. Sienkiewicz, B. Zhao, The modern-era retrospective analysis for Research and applications, version 2 (MERRA-2), J. Clim. 30 (2017) 5419–5454.
[33] T.J. Silverman, M.G. Deceglie, B. Marion, S. Cowley, B. Kayes, S. Kurtz, Outdoor performance of a thin-film gallium-arsenide photovoltaic module, in: 2013 IEEE 39th Photovoltaic Specialists Conference (PVSC), 2013, pp. 103–108.
[34] T. Hubert, E. Vidalenc, Renewable electricity potentials in France: a long term perspective, Energy Proc. 20 (2012) 247–257.